PAPER • **OPEN ACCESS**

Electronic *g*-tensors of dangling bonds in hydroxylated and aminated nanodiamonds: a computational study

To cite this article: Šarūnas Masys *et al* 2025 *Phys. Scr.* **100** 015402

Physica Scripta

PAPER

Electronic *g*-tensors of dangling bonds in hydroxylated and aminated nanodiamonds: a computational study

Šarūnas Masys[1], **Valdas Jonauskas**[1] and **Zilvinas Rinkevicius**[2]

[1] Institute of Theoretical Physics and Astronomy, Faculty of Physics, Vilnius University, LT-10257 Vilnius, Lithuania
[2] Department of Theoretical Chemistry and Biology, School of Engineering Sciences in Chemistry, Biotechnology and Health, KTH Royal Institute of Technology, SE-10691 Stockholm, Sweden

E-mail: Sarunas.Masys@tfai.vu.lt

Keywords: electronic *g*-tensor, dangling bonds, nanodiamonds

OPEN ACCESS

RECEIVED
31 July 2024

REVISED
10 November 2024

ACCEPTED FOR PUBLICATION
20 November 2024

PUBLISHED
2 December 2024

Abstract

The calculations of electronic *g*-tensors, one of the most important parameters in electron paramagnetic resonance spectroscopy, are carried out for dangling bonds (DBs) introduced into hydroxylated and aminated diamond nanoparticles, or nanodiamonds (NDs), of different shapes and sizes. Regarding the shapes of NDs, octahedral, cubic, and tetrahedral model systems are used, while the impact of the change in size is inspected by increasing octahedral ND from C_{35} to C_{84}. The results for single DBs reveal that tetrahedral NDs exhibit the widest variation range of the isotropic *g*-shift values for both surface functionalization schemes, whereas the isotropic *g*-shifts of octahedral and cubic NDs tend to strongly overlap. On the other hand, if one treats NDs as an ensemble of nanoparticles constituting a sample, the isotropic *g*-shifts arithmetically averaged over all available DBs show that tetrahedral ND with hydroxylated surface possesses a significantly higher value than the rest of the considered systems. However, applying the Boltzmann distribution results in a substantially lower value for cubic ND. In contrast, aminated NDs do not demonstrate average values that stand out from the others, irrespective of the analysis method employed. Overall, in addition to the comprehensive magnetic properties, the obtained data also provide interesting details on the formation of DBs in hydroxylated and aminated NDs.

1. Introduction

Among a large variety of nanoparticles potentially attractive for the nanomedicine applications [1–3], carbon-based nanodiamonds (NDs), in addition to the other beneficial properties [4], are able to offer low toxicity [5], good biocompatibility [6], and high photostability [7]. These features are particularly desirable for the effective non-invasive bioimaging which, in turn, is essential in enhancing the pre-clinical diagnosis and therapy [8], especially in the field of cancer [9]. It should be noted that, besides the techniques that rely on fluorescence microscopy [10] or soft x-ray tomography [11], NDs can also be visualized using magnetic resonance imaging (MRI)—a tool which is highly valued for its excellent spatial resolution and lack of ionizing radiation [12]. However, neither direct [13] nor indirect [14] detection of NDs via MRI would be possible without the presence of a suitable paramagnetic reservoir necessary for the electron spin polarization transfer to the appropriate nuclei. Having in mind that carbon dangling bonds (DBs) are one of the most abundant paramagnetic defects in NDs [15–17], it is very likely that they have a huge impact on the ability to visualize NDs in the MRI scans [13, 14]. Therefore, we find it important to conduct the research on these unpaired carbon electrons located at the surface of NDs.

In our previous paper dedicated for DBs in NDs [18], a focus was put on hydrogenated and fluorinated NDs of different shapes and sizes, while for hydroxylated and aminated NDs only the smallest model (C_{35}) of the most common octahedral shape [19] was applied. In this work, we would like to expand the aforementioned investigation on DBs by encompassing more model systems for hydroxylated and aminated NDs. It is worthwhile mentioning that hydroxylation and amination are commercially available surface functionalization

schemes [20], besides, hydroxyl group dominates the surface of the high-pressure high-temperature NDs [21] and hydroxylated NDs themselves can enable a broad variety of useful subsequent functionalizations like silylation or acylation [22]. Aminated NDs, on the other hand, are of high interest for the theranostic applications due to the possibility to conjugate various functional biomolecules via amide chemistry, nucleophilic substitution, or condensation reactions [22]. In general, the shape, size, and surface functionalization of nanoparticles have a profound impact on their transport, adhesion, and biodistritubion [23]—critical properties in the area of nanomedicine. The study of differently shaped and sized NDs with hydroxylated and aminated surfaces contributes to the efforts to get a wider picture of the behaviour inherent for NDs.

The suitability of paramagnetic impurities for the visualization of NDs employing MRI can be checked by the electron paramagnetic resonance (EPR) measurements [13, 14, 24]. EPR is considered as a primary tool to directly observe paramagnetic defects [17] and electronic *g*-tensor is one of its key parameters containing a wealth of information about the electronic and geometrical structure of the investigated systems [25–27]. Needless to say, the accurate determination of *g*-tensor values—both experimentally and computationally—is essential for the precise interpretation of EPR spectra and the proper identification of distinct paramagnetic species present in NDs. Since NDs might be produced in various shapes, not to mention sizes [28], we have evaluated the *g*-tensor dependence on the shape as well as size for hydroxylated and aminated NDs with introduced DBs. To be concrete, the *g*-tensor calculations were performed for octahedral, cubic, and tetrahedral NDs, whereas the impact of the change in size was tested by increasing octahedrally-shaped ND from C_{35} (∼0.9 nm) to C_{84} (∼1.2 nm). Given that high quality NDs as small as 1.1 nm were successfully produced in the laboratory [29], our research is not only theoretically significant—it actually broadens the knowledge about the magnetic properties of DBs in experimentally realizable NDs. In addition, it also reveals interesting details on their formation hardly visible to the experiment. On the whole, small size of NDs might be advantageous in nanomedicine applications since it facilitates ND penetration through narrow pores in biological structures like nucleolemma and kidney filtration system [30], or blood-brain barrier [31]. But with the smaller size the reliable characterization becomes rather problematic because the properties of such NDs deviate from the known properties and characteristics of bulk diamond and even larger NDs, making correct assignment of the analytical signals complicated [32]. We believe that the obtained theoretical data and its interpretation will be useful in analyzing, identifying, and explaining the results of EPR measurements on NDs.

2. Computational details

The geometry optimization was carried out with the ultrafast GFN2-xTB method [33] via xtb (version 6.4.1) program package [34] exploiting it as an external ORCA (version 4.2.1) program system module [35, 36]. GFN2-xTB relies strictly on element-specific (not element pair-specific) and global parameters that were fitted to yield reasonable structures, vibrational frequencies, and non-covalent interactions for molecules across the periodic table. The main focus of this method are organic, organometallic, and biochemical systems, with sizes potentially exceeding a few thousand atoms [33]. Our previous investigation [37], partly dedicated for the DBs in hydroxylated and aminated NDs, has revealed that despite its semiempirical tight-binding nature GFN2-xTB was able to provide results perfectly comparable to those of the much more robust hybrid density functional theory (DFT) based scheme like PBE0/def2-TZVP [38, 39]. This finding allowed us to save a huge amount of computational time and resources while optimizing geometry in the current study. To maintain the high level of precision, the convergence criteria for the single-point calculations as well as geometry relaxation procedures were tightened as it was done previously [18, 37, 40–42]. To be concrete, the geometry optimization was considered complete when five parameters satisfied the determined thresholds (in atomic units): the change in energy ($1 \cdot 10^{-6}$), the root-mean-square values of gradients ($3 \cdot 10^{-5}$) and displacements ($6 \cdot 10^{-4}$), the largest values of gradients ($1 \cdot 10^{-4}$) and displacements ($1 \cdot 10^{-3}$). In addition, the optimization was performed in redundant internal coordinates using a quasi-Newton algorithm of BFGS type [43]. Concerning the accuracy thresholds of the single-point calculations, they were respectively set to 32, $2 \cdot 10^{-9}$, $2 \cdot 10^{-7}$, and $2 \cdot 10^{-5}$ for the parameters defining integral cutoff, integral neglect, self-consistent charge convergence, and wavefunction convergence. DBs were introduced into geometrically optimized NDs by removing appropriate OH or NH_2 groups—single at a time—and then reoptimizing geometry of the resulting systems. All drawings were produced with the visualization program VESTA [44].

The energetic analysis and electronic *g*-tensor calculations were conducted using the thoroughly tested [40] combination of B3LYP/6-311G(2d,2p) [45–48]. Although the default values were selected for most of the technical ORCA setup, DFT integration grid for the tightened self-consistent field (SCF) procedure was increased (keyword GRID7), whereas grid for the final energy evaluation was turned off. To reduce the computational time with the minimal loss of precision, modified resolution of the identity (RI) [49] and chain of

spheres (COS) [50] techniques, commonly known as RIJCOSX approximation, were applied for the Coulomb and Hartree–Fock exchange interactions, respectively. An auxiliary Coulomb-fitting basis set was generated automatically [51]. For the sake of greater accuracy while utilizing the gauge-including atomic orbitals within the effective nuclear charge framework [52–54], default COS grid was substantially expanded (keyword GRIDX9) and the final one was withdrawn.

From the experimental perspective, EPR measurements are interpreted by adopting the spin Hamiltonian (SH) concept [55] which allows to summarize the observed spectra into a set of phenomenological parameters. In other words, EPR spectroscopists are able to perform analysis by applying the least-squares fitting of SH parameters to experimental data and thereby extract the SH values of interest [56]. Being one of the central SH parameters, g-tensor describes the Zeeman interaction between an external magnetic field $\overrightarrow{\mathrm{B}}$ and an effective spin $\overrightarrow{\mathrm{S}}$ of the system [57]:

$$\hat{H}_{\mathrm{SH}} = \mu_{\mathrm{B}} \overrightarrow{\mathrm{B}} \cdot \mathbf{g} \cdot \hat{\overrightarrow{\mathrm{S}}}, \tag{1}$$

where μ_{B} and $\mathbf{g}$ correspondingly denote the Bohr magneton and g-tensor. From a theoretical point of view, this quantity can be derived from the quantum chemistry calculations utilizing a variety of techniques [58–62]. In this work, a coupled-perturbed SCF treatment was employed allowing the usage of hybrid DFT functionals [59]. As for the calculations, the isotropic g-shift values (or simply the isotropic g-shifts) $\triangle\overline{g}$ were computed by subtracting the free electron g-factor ($g_{\mathrm{e}} = 2.0023193$) from the isotropic g-tensor values $\overline{g}$ and expressing the difference in parts per million (ppm). $\overline{g}$ were taken as an arithmetic average of the principal components g_{ii} ($i = x, y, z$) which, in turn, were obtained as the positive square roots of the eigenvalues of $\mathbf{g}^{\mathrm{T}} \cdot \mathbf{g}$.

3. Results and discussion

The visual representation of hydroxylated and aminated NDs can be found in figures 1 and 2, respectively. The results of the electronic g-tensor calculations for their DBs are correspondingly provided in figures 3 and 4. We would like to emphasize that, in contrast to hydrogenated or fluorinated NDs, the g-tensor needs to be evaluated for all possible DB positions in hydroxylated and aminated NDs, since in such systems due to their spatially more complex surface structure no geometrically equivalent DBs might exist. Trying to estimate only a few g-tensor values for the randomly selected set of DBs will not give a complete picture of this type of magnetic behaviour. Therefore, we have performed 36 (C_{35}), 64 (C_{84}), 52 (C_{51}), and 48 (C_{54}) g-tensor calculations for each of the investigated surface functionalization scheme thereby taking into consideration all possible DBs.

Now let us take a closer look at figure 3 with the results of hydroxylated NDs. Probably the first thing that catches the eye is the distribution of the isotropic g-shifts for tetrahedral $C_{51}(OH)_{52}$, as one can easily distinguish three groups of DBs having similar $\triangle\overline{g}$ values. From the geometrical point of view, the first group (−135 to −96 ppm) consists of DBs located at the vertices of ND, the second group (702 to 800 ppm) is made of DBs situated at the facets of ND, whereas DBs from the third group (955 to 1208 ppm) are positioned at the edges of ND. This finding actually confirms our previous observation on the octahedrally-shaped NDs [18] according to which hydroxylated and aminated systems do not possess geometrically equivalent DBs but, despite that, they do possess geometrically similar ones. It basically means that although the energies of these DBs may be very dissimilar, the geometric similarity in some cases can be clearly reflected by their isotropic g-shifts falling within certain ranges of values. Concerning the whole variation range of $\triangle\overline{g}$, its span of 1343ppm (-135 to 1208 ppm) is the widest among all considered nanoparticles in the current work and somewhat reminds that of fluorinated NDs [18]. After stating this, it goes without saying that octahedral $C_{35}(OH)_{36}$ and $C_{84}(OH)_{64}$ show a lower variation range of $\triangle\overline{g}$: 967 ppm (142 to 1109 ppm) is demonstrated by the former and 790 ppm (285 to 1075 ppm) is exhibited by the latter. These numbers also indicate that an increase in octahedral NDs size resulted in a slight decrease in their $\triangle\overline{g}$ range. In addition, neither $C_{35}(OH)_{36}$ nor $C_{84}(OH)_{64}$ displays $\triangle\overline{g}$ values which are below the lower bound (−135 ppm) or above the upper bound (1208 ppm) given by tetrahedral ND. The same is true talking about cubic $C_{54}(OH)_{48}$, since its lowest (29 ppm) as well as highest (1103 ppm) isotropic g-shifts also fall within the range defined by the lower and upper bounds of $C_{51}(OH)_{52}$. But to be precise, its variation range of $\triangle\overline{g}$ (1074 ppm) is a bit wider than that of $C_{35}(OH)_{36}$, not to mention $C_{84}(OH)_{64}$. Taking all these observations into account, it is obvious that the results of octahedral and cubic NDs are strongly overlapped almost throughout the whole range of their isotropic g-shifts. Starting from ∼700 ppm, DBs introduced into tetrahedral ND produce a large amount of overlapping $\triangle\overline{g}$ values too. However, the most intriguing thing that should be pointed out is the isotropic g-shifts of the lowest energy DBs (represented by the black-colored symbols). One can note that these $\triangle\overline{g}$ values for smaller octahedral (1066 ppm), larger octahedral (1040 ppm), and tetrahedral (1203 ppm) NDs are not too distinct but the corresponding value for cubic ND (327 ppm) definitely stands out. From the geometrical perspective (see figure 1), the lowest energy DBs in tetrahedral as well as both octahedral systems are irregular, that is, formed of the OH-bonded (or NH_2-bonded for aminated

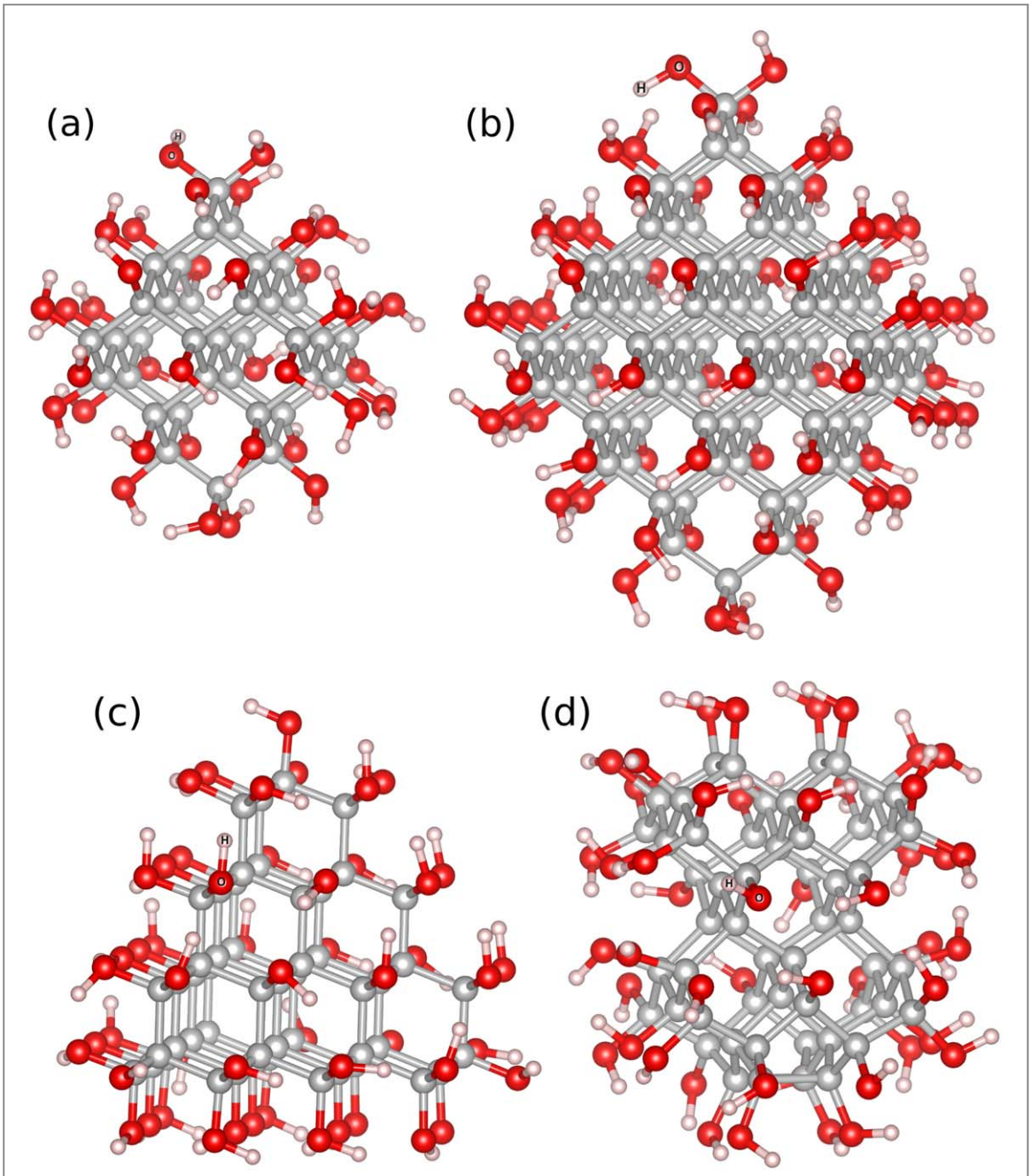

Figure 1. Visual representation of hydroxylated NDs: octahedral (a) $C_{35}(OH)_{36}$ and (b) $C_{84}(OH)_{64}$ as well as (c) tetrahedral $C_{51}(OH)_{52}$ and (d) cubic $C_{54}(OH)_{48}$. Grey, red, and pink balls stand for carbon, oxygen, and hydrogen atoms, respectively. The labelled atoms are the ones that should be removed to obtain the lowest energy DB.

surfaces) dangling C atom, and this apparently contrasts with cubic ND where the lowest energy DB is regular, that is, composed of a dangling C atom bonded by no other atoms than C. Such finding reveals that the lowest energy DBs in hydroxylated diamond nanoparticles are not necessarily of an irregular type, as would be suggested by an analysis of our results for octahedral and/or tetrahedral NDs only. It is interesting to notice though that irregular DBs in hydrogenated and fluorinated NDs of octahedral shape were found to be the most energetically unfavorable among all available DBs [18], indicating how diversely different surface functionalization schemes may behave.

The results of *g*-tensor calculations for DBs in aminated NDs, graphically summarized in figure 4, show that tetrahedral $C_{51}(NH_2)_{52}$ possesses the widest span of $\triangle\overline{g}$ values (889 ppm), however, it is narrower compared to that of tetrahedrally-shaped ND with hydroxylated surface (1343 ppm). What is more, the isotropic *g*-shifts for DBs at the edges (424 to 671 ppm) and facets (626 to 909 ppm) of ND are hardly distinguishable and appear to be reversed in terms of the order one could previously see for $C_{51}(OH)_{52}$ exhibiting lower values for DBs at the facets (702 to 800 ppm) and higher values for DBs at the edges (955 to 1208 ppm). Despite these differences, $\triangle\overline{g}$ for DBs at the vertices (20 to 43 ppm) remain clearly separated from the values for DBs at the edges and facets.

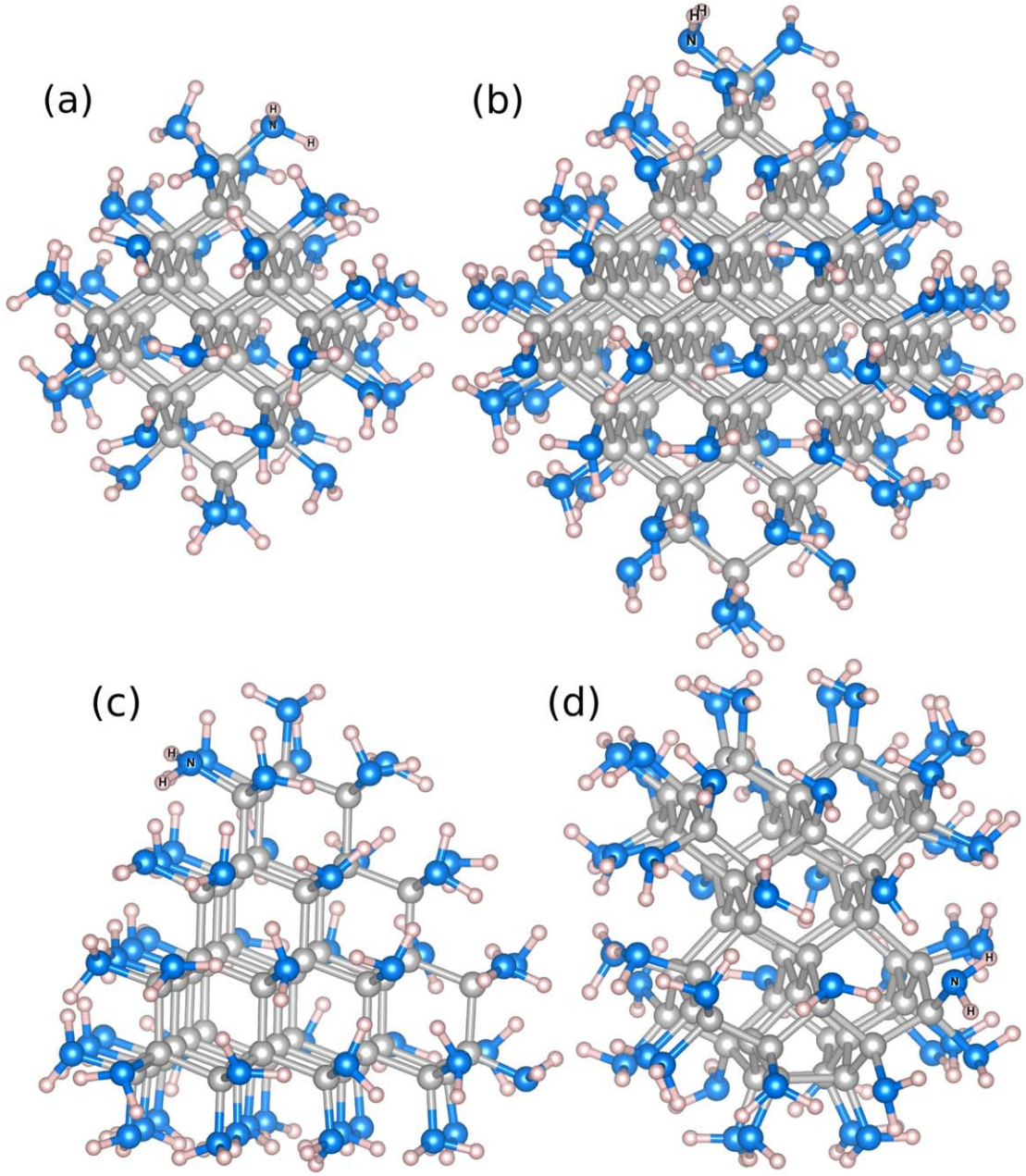

Figure 2. Visual representation of aminated NDs: octahedral (a) $C_{35}(NH_2)_{36}$ and (b) $C_{84}(NH_2)_{64}$ as well as (c) tetrahedral $C_{51}(NH_2)_{52}$ and (d) cubic $C_{54}(NH_2)_{48}$. Grey, azure, and pink balls stand for carbon, nitrogen, and hydrogen atoms, respectively. The labelled atoms are the ones that should be removed to obtain the lowest energy DB.

Needless to say, the variation ranges of $\triangle\overline{g}$ for octahedral $C_{35}(NH_2)_{36}$ and $C_{84}(NH_2)_{64}$ are lower in comparison to $C_{51}(NH_2)_{52}$: 314 ppm (277 to 591 ppm) can be noted for the former and 548 ppm (319 to 867 ppm) for the latter. It is obvious as well that none of these octahedral NDs demonstrate $\triangle\overline{g}$ values which are below the lower bound (20 ppm) or above the upper bound (909 ppm) determined by tetrahedral ND. But an interesting thing though is the trend related to the change in size which contrasts with the behaviour observed for the hydroxylated surface, since an increase in octahedral NDs size now results in an increase, not a decrease, in the variation range of their isotropic *g*-shifts. And $\triangle\overline{g}$ range for $C_{84}(NH_2)_{64}$ is actually slightly wider than that for cubic $C_{54}(NH_2)_{48}$ (533 ppm), whose lowest (131 ppm) and highest (664 ppm) values also fall within the range confined by the lower and upper bounds of tetrahedral ND. Concerning the tendency related to the overlap of the results, it does not seem to be too different from the one seen for hydroxylated systems, except that the heaviest overlap is present at somewhat lower $\triangle\overline{g}$ range from ~400 to ~600 ppm. The lowest energy DBs, on the other hand, are all irregular, including even cubic ND (see figure 2), and it is therefore not very surprising that their isotropic *g*-shifts are quite similar—529 ppm for $C_{35}(NH_2)_{36}$, 580 ppm for $C_{54}(NH_2)_{48}$, 583 ppm for $C_{51}(OH)_{52}$, and 608 ppm for $C_{84}(NH_2)_{64}$. Nevertheless, we would like to stress that in general one should not

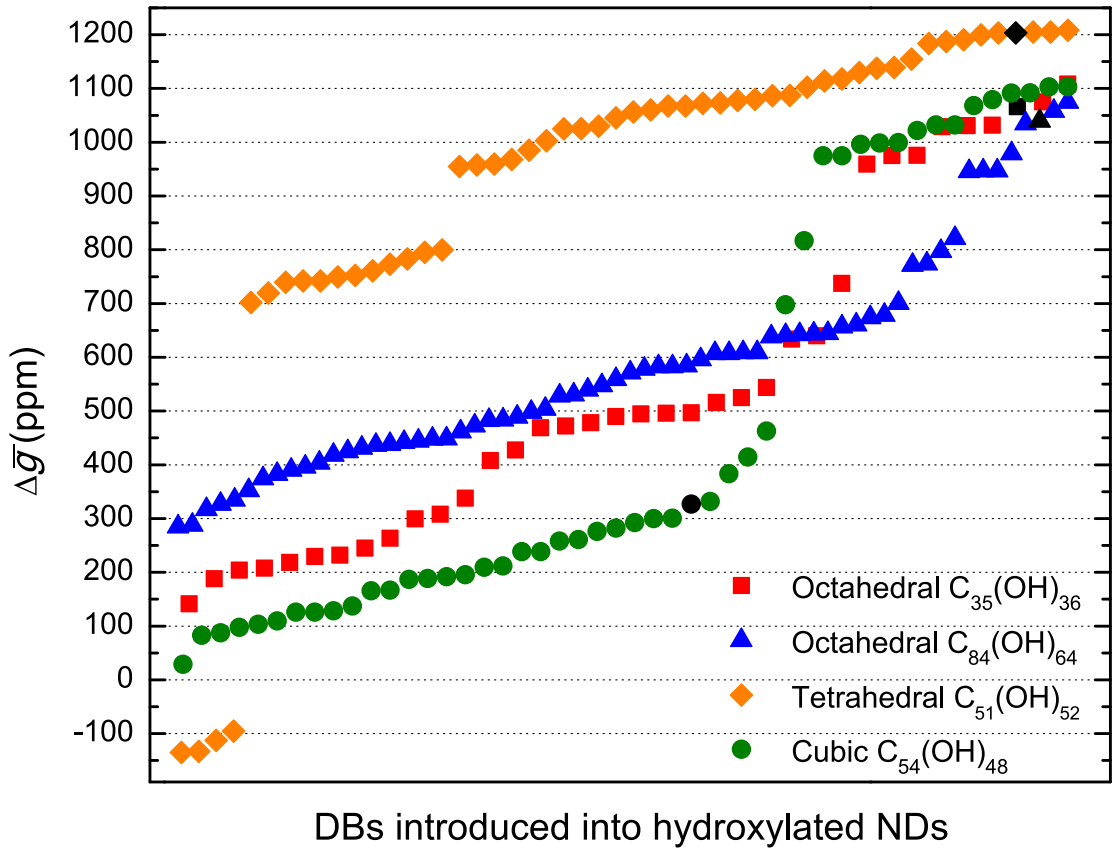

Figure 3. Isotropic *g*-shifts $\Delta\overline{g}$ calculated for all possible DB positions in hydroxylated NDs. Black-colored symbols represent the lowest energy DBs.

rule out the possibility to deal with the lowest energy DBs of a regular type, as they could be inherent for aminated NDs of other shapes and/or sizes which were not considered in the current study.

It is evident that the preceding data analysis focuses on the results for single NDs, while experimentally an average value of $\Delta\overline{g}$ for an ensemble of nanoparticles that constitute a sample is observed [63]. In order to take this into account, let us make a simplifying assumption that the ensembles of NDs are formed by diamond nanoparticles of the same shape and size. This does not sound unrealistic, given that the centrifugation process may be shape-dependent, possibly separating nanoparticles not only of different sizes but also of different shapes [64]. Having in mind that it is common to apply such processes as crushing, grinding, or nanomilling during the fabrication procedure of NDs [63], one could make another assumption that the formation of their DBs might occur in a random statistical manner. That being said, we have averaged isotropic *g*-shifts over all DBs available in a particular ND and the obtained results are listed in table 1. Here, it can be noted that the arithmetic averages of $\Delta\overline{g}$ for smaller octahedral (554 ppm), larger octahedral (587 ppm), and cubic (479 ppm) NDs with hydroxylated surfaces are rather similar but the respective arithmetic average for tetrahedral ND (922 ppm) is considerably higher. On the other hand, the arithmetically averaged $\Delta\overline{g}$ for tetrahedral ND with aminated surface (557 ppm) does not stand out from the corresponding values demonstrated by smaller octahedral (462 ppm), larger octahedral (580 ppm), and cubic (403 ppm) NDs. In general, one can state that the results of hydroxylated nanoparticles appear to be higher than the respective results of aminated NDs.

The assumption that the formation of DBs might occur in a random statistical manner does not take into consideration their total energy distribution or, simply speaking, the fact that total energies of some DBs are noticeably higher compared to the others. In order to reveal the impact of this factor, we have estimated the formation probabilities of DBs via Boltzmann distribution at a temperature of 300 K and employed them while calculating the average value of $\Delta\overline{g}$ for a particular ND. As with the arithmetic averages, the evaluated Boltzmann-weighted averages can also be found in table 1. But before going deeper, we would like to point out the influence the lowest energy DBs have on the obtained results. Regarding the hydroxylated systems, the formation probability of the lowest energy DB is 0.91 for smaller octahedral, 0.85 for larger octahedral, 0.44 for tetrahedral, and 0.99 for cubic NDs, whereas in case of amination the corresponding values are 0.67, 0.36, 0.65, and 0.99. The given numbers actually imply that the contribution of the lowest energy DBs to the Boltzmann-weighted average of isotropic *g*-shifts is truly significant and for some NDs even absolutely dominant, and this is the reason why we

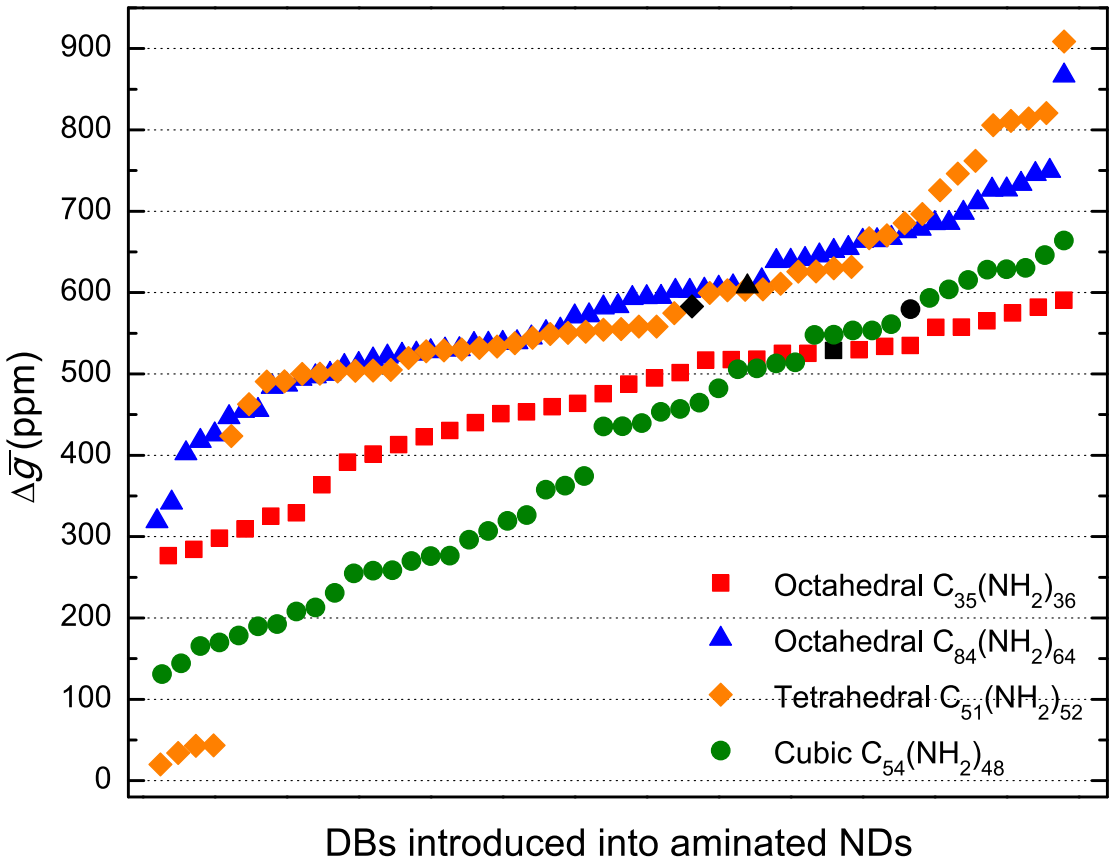

Figure 4. Isotropic *g*-shifts $\Delta\overline{g}$ calculated for all possible DB positions in aminated NDs. Black-colored symbols represent the lowest energy DBs.

Table 1. Isotropic *g*-shifts $\Delta\overline{g}$ (in ppm) averaged over all DBs introduced into a particular hydroxylated or aminated ND.

	Hydroxylated		Aminated	
NDs	Arithmetic average	Boltzmann average	Arithmetic average	Boltzmann average
Octahedral C_{35}	554	1060	462	528
Octahedral C_{84}	587	991	580	586
Tetrahedral C_{51}	922	1180	557	605
Cubic C_{54}	479	327	403	579

have highlighted these DBs in our previous analysis on data provided in figures 3 and 4. Now let us get back to table 1. Concerning the hydroxylated nanoparticles, one can find that the application of Boltzmann distribution results in substantially increased averages for smaller octahedral (1060 ppm) as well as larger octahedral (991 ppm) NDs. A smaller increase is also observed for tetrahedral ND (1180 ppm), however, a decrease compared to an arithmetic average is demonstrated by cubic ND (327 ppm), and this considerably lower number makes cubic system stand out from the rest of the hydroxylated nanoparticles. But despite such trend, cubic ND with aminated surface does not distinguish from other aminated NDs, as its Boltzmann-weighted average of $\Delta\overline{g}$ (579 ppm) is very similar to the respective values estimated for smaller octahedral (528 ppm), larger octahedral (586 ppm), and tetrahedral (605 ppm) NDs. In addition, an employment of Boltzmann distribution tends to increase the averages of isotropic *g*-shifts for all aminated NDs, with cubic ND being affected the most. One may also notice that, compared to the results of hydroxylated systems, the corresponding numbers of aminated nanoparticles seem to be lower, except for the cubic ND. On the whole, we would like to emphasize that the averages of $\Delta\overline{g}$ show a negligible dependence on the size of hydroxylated NDs but the sensitivity to the change in shape is clearly pronounced, regardless of the analysis method used. Aminated NDs, on the other hand, behave quite differently, since their

averages of isotropic g-shifts do not exhibit such a clearly expressed dependence on the shape of NDs, while sensitivity to the change in size is not negligible but still can be considered as weak.

From the experimental perspective, a typical $\triangle\overline{g}$ value associated with DBs in NDs (of an unspecified surface functionalization, unfortunately) is $\sim 480 \pm 200$ ppm [16]. By comparing this number to the numbers presented in table 1, one can note that the results of aminated NDs fall within the range defined by the lower (~280 ppm) and upper (~680 ppm) bounds of experimental estimates. But the same cannot be said about hydroxylated nanoparticles, as only the values of cubic system fully agree with the experimental measurements, while Boltzmann-weighted averages for the rest of NDs are too high. And the fact that an arithmetic average of tetrahedral ND also exceeds the upper experimental limit raises an interesting question whether EPR measurements conducted solely on hydroxylated NDs would show $\triangle\overline{g}$ values different from the ones typically associated with DBs in NDs. It seems that there might be some potential for this to happen.

It is also interesting to take a look at values inherent for DBs in other systems with chemically similar elements. As an example, EPR measurements on DBs in the hydrogenated amorphous silicon show $\triangle\overline{g}$ of $\sim 3480 \pm 200$ ppm [65], while DBs located at the interface of Ge/GeO_2 possess $\triangle\overline{g}$ of $\sim 9350 \pm 400$ ppm [66]. These numbers clearly indicate that it is highly unlikely to confuse DBs in NDs with DBs in Si- or Ge-based materials.

4. Conclusions

In this paper, the electronic g-tensor calculations were performed for DBs introduced into hydroxylated and aminated NDs of different shapes and sizes. It is revealed that tetrahedrally-shaped NDs demonstrate the widest span of the isotropic g-shift values for both surface functionalization schemes, while isotropic g-shifts of octahedral and cubic NDs strongly overlap. However, cubic ND with hydroxylated surface possesses the lowest energy DB of a regular type, contrasting with other investigated systems for which the lowest energy DBs are irregular. The difference in behaviour is also seen regarding the change in size, as an increase from C_{35} to C_{84} decreases the variation range of the isotropic g-shift values for hydroxylated NDs, but an increase is exhibited by aminated NDs. In case NDs are treated as an ensemble of nanoparticles constituting a sample, the isotropic g-shifts arithmetically averaged over all available DBs show that tetrahedral ND with hydroxylated surface stands out from the rest of the considered systems, as its result is higher compared to the experimental findings for DBs in NDs of an unspecified surface functionalization. And if Boltzmann distribution is taken into account, in addition to the aforementioned tetrahedral ND, octahedrally-shaped systems with hydroxylated surface also apparently exceed EPR measurements, while aminated NDs agree with the experimental data within the margins of error. The sensitivity to the change in size, on the other hand, can be considered as weak for both surface functionalization schemes, irrespective of the analysis method applied.

Data availability statement

The data cannot be made publicly available upon publication because the cost of preparing, depositing and hosting the data would be prohibitive within the terms of this research project. The data that support the findings of this study are available upon reasonable request from the authors.

ORCID iDs

Šarūnas Masys https://orcid.org/0000-0003-0004-1104
Valdas Jonauskas https://orcid.org/0000-0002-5035-6270
Zilvinas Rinkevicius https://orcid.org/0000-0003-2729-0290

References

[1] Zhang L, Gu F X, Chan J M, Wang A Z, Langer R S and Farokhzad O C 2008 Nanoparticles in medicine: therapeutic applications and developments *Clin. Pharmacol. Ther.* **83** 761
[2] Chow E K-H and Ho D 2013 Cancer nanomedicine: from drug delivery to imaging *Sci. Transl. Med.* **5** 216rv4
[3] Selim M M, El-Safty S, Tounsi A and Shenashen M 2024 A review of magnetic nanoparticles used in nanomedicine *APL Mater* **12** 010601
[4] Nunn N, Torelli M, McGuire G and Shenderova O 2017 Nanodiamond: a high impact nanomaterial *Curr. Opin. Solid St. M.* **21** 1
[5] Yuan Y, Wang X, Jia G, Liu J-H, Wang T, Gu Y, Yang S-T, Zhen S, Wang H and Liu Y 2010 Pulmonary toxicity and translocation of nanodiamonds in mice *Diam. Relat. Mater.* **19** 291
[6] Barone F C, Marcinkiewicz C, Li J, Feng Y, Sternberg M, Lelkes P I, Rosenbaum-Halevi D, Gerstenhaber J A and Feuerstein G Z 2019 Long-term biocompatibility of fluorescent diamonds-(NV)-$Z \sim 800$ nm in rats: survival, morbidity, histopathology, and particle distribution and excretion studies (part IV) *Int. J. Nanomed.* **14** 1163

[7] Sow M, Steuer H, Adekanye S, Gins L, Mandal S, Gilboa B, Williams O A, Smith J M and Kapanidis A N 2020 High-throughput nitrogen-vacancy center imaging for nanodiamond photophysical characterization and pH nanosensing *Nanoscale* **12** 21821
[8] Fryer C, Murray P and Zhang H 2024 Modification of nanodiamonds for fluorescence bioimaging *RSC Adv.* **14** 4633
[9] Priyadarshni N, Singh R and Mishra M K 2024 Nanodiamonds: next generation nano-theranostics for cancer therapy *Cancer Lett* **587** 216710
[10] Yu S-J, Kang M-W, Chang H-C, Chen K-M and Yu Y-C 2005 Bright fluorescent nanodiamonds: no photobleaching and low cytotoxicity *J. Am. Chem. Soc.* **127** 17604
[11] Reineck P *et al* 2021 Multimodal imaging and soft X-ray tomography of fluorescent nanodiamonds in cancer cells *Biotechnol. J.* **16** 2000289
[12] Dey T *et al* 2024 Surface engineered nanodiamonds: mechanistic intervention in biomedical applications for diagnosis and treatment of cancer *Biomed. Mater.* **19** 032003
[13] Waddington D E J *et al* 2017 Nanodiamond-enhanced MRI via *in situ* hyperpolarization *Nat. Commun.* **8** 15118
[14] Waddington D E J, Boele T, Rej E, McCamey D R, King N J C, Gaebel T and Reilly D J 2019 Phase-encoded hyperpolarized nanodiamond for magnetic resonance imaging *Sci. Rep.* **9** 5950
[15] Panich A M 2012 Nuclear magnetic resonance studies of nanodiamonds *Crit. Rev. Solid State Mater. Sci.* **37** 276
[16] Panich A M, Sergeev N A, Shames A I, Osipov V Y, Boudou J-P and Goren S D 2015 Size dependence of ^{13}C nuclear spin-lattice relaxation in micro- and nanodiamonds *J. Phys.: Condens. Matter* **27** 072203
[17] Panich A M, Sergeev N A and Goren S D 2020 Location of paramagnetic defects in detonation nanodiamond from proton spin-lattice relaxation data *Solid State Nucl. Magn. Reson.* **105** 101624
[18] Masys Š, Jonauskas V and Rinkevicius Z 2021 Electronic g-tensor calculations for dangling bonds in nanodiamonds *J. Phys. Chem. A* **125** 8249
[19] Barnard A S 2013 Modeling polydispersive ensembles of diamond nanoparticles *Nanotechnology* **24** 085703
[20] Chipaux M, van der Laan K J, Hemelaar S R, Hasani M, Zheng T and Schirhagl R 2018 Nanodiamonds and their applications in cells *Small* **14** 1704263
[21] Wolcott A, Schiros T, Trusheim M E, Chen E H, Nordlund D, Diaz R E, Gaathon O, Englund D and Owen J S 2014 Surface structure of aerobically oxidized diamond nanocrystals *J. Phys. Chem.* C **118** 26695
[22] Pramanik G, Bag S and Chakrabortty S 2022 Fluorescent nanodiamond for nanotheranostic applications *Microchim. Acta* **189** 447
[23] Liu Y, Tan J, Thomas A, Ou-Yang D and Muzykantov V R 2012 The shape of things to come: importance of design in nanotechnology for drug delivery *Ther. Deliv.* **3181**
[24] Rej E, Gaebel T, Boele T, Waddington D E J and Reilly D J 2015 Hyperpolarized nanodiamond with long spin-relaxation times *Nat. Commun.* **6** 8459
[25] Barone V and Cimino P 2009 Validation of the B3LYP/N07D and PBE0/N07D computational models for the calculation of electronic g-tensors *J. Chem. Theory Comput.* **5** 192
[26] Tran V A and Neese F 2020 Double-hybrid density functional theory for g-tensor calculations using gauge including atomic orbitals *J. Chem. Phys.* **153** 054105
[27] Niklas J, Mardis K L and Poluektov O G 2018 Spin signature of the C_{60} fullerene anion: a combined X- and D-band EPR and DFT study *J. Phys. Chem. Lett.* **9** 3915
[28] Shenderova O A and McGuire G E 2015 Science and engineering of nanodiamond particle surfaces for biological applications (Review) *Biointerphases* **10** 030802
[29] Stehlik S *et al* 2015 Size and purity control of HPHT nanodiamonds down to 1 nm *J. Phys. Chem.* C **119** 27708
[30] Turcheniuk K and Mochalin V N 2017 Biomedical applications of nanodiamond (Review) *Nanotechnology* **28** 252001
[31] Bhogale D, Mazahir F and Yadav A K 2022 Recent synergy of nanodiamonds: role in brain-targeted drug delivery for the management of neurological disorders *Mol. Neurobiol.* **59** 4806
[32] Chang S L Y, Reineck P, Krueger A and Mochalin V N 2022 Ultrasmall nanodiamonds: perspectives and questions *ACS Nano* 168513
[33] Bannwarth C, Ehlert S and Grimme S 2019 GFN2-xTB—An accurate and broadly parametrized self-consistent tight-binding quantum chemical method with multipole electrostatics and density-dependent dispersion contributions *J. Chem. Theory Comput.* **15** 1652
[34] Bannwarth C, Caldeweyher E, Ehlert S, Hansen A, Pracht P, Seibert J, Spicher S and Grimme S 2021 Extended tight-binding quantum chemistry methods *WIREs Comput. Mol. Sci.* **11** e1493
[35] Neese F 2012 The ORCA program system *WIREs Comput. Mol. Sci.* **2** 73
[36] Neese F 2018 Software update: the ORCA program system, version 4.0 *WIREs Comput. Mol. Sci.* **8** e1327
[37] Masys Š, Jonauskas V and Rinkevicius Z 2023 Geometries of defects in nanodiamonds optimized with the low-cost methods: how good are they for the electronic g-tensor calculations? *Diam. Relat. Mater.* **136** 110009
[38] Adamo C and Barone V 1999 Toward reliable density functional methods without adjustable parameters: the PBE0 model *J. Chem. Phys.* **110** 6158
[39] Weigend F and Ahlrichs R 2005 Balanced basis sets of split valence, triple zeta valence and quadruple zeta valence quality for H to Rn: design and assessment of accuracy *Phys. Chem. Chem. Phys.* **7** 3297
[40] Masys Š, Rinkevicius Z and Tamulienė J 2019 On the magnetic properties of nanodiamonds: electronic g-tensor calculations *J. Chem. Phys.* **151** 044305
[41] Masys Š, Rinkevicius Z and Tamulienė J 2019 Electronic g-tensors of nanodiamonds: dependence on the size, shape, and surface functionalization *J. Chem. Phys.* **151** 144305
[42] Masys Š, Rinkevicius Z and Tamulienė J 2020 Computational study on the electronic g-tensors of hydrophilic and hydrophobic nanodiamonds interacting with water *J. Chem. Phys.* **152** 144302
[43] Nocedal J and Wright S J 2006 *Numerical optimization, Chapter 6: Quasi-Newton methods* Springer 135–63
[44] Momma K and Izumi F 2011 VESTA3 for three-dimensional visualization of crystal, volumetric and morphology data *J. Appl. Crystallogr.* **44** 1272
[45] Becke A D 1993 Density-functional thermochemistry. III. The role of exact exchange *J. Chem. Phys.* **98** 5648
[46] Stephens P J, Devlin F J, Chabalowski C F and Frisch M J 1994 Ab initio calculation of vibrational absorption and circular dichroism spectra using density functional force fields *J. Phys. Chem.* **98** 11623
[47] Krishnan R, Binkley J S, Seeger R and Pople J A 1980 Self-consistent molecular orbital methods. XX. A basis set for correlated wave functions *J. Chem. Phys.* **72** 650
[48] Frisch M J, Pople J A and Binkley J S 1984 Self-consistent molecular orbital methods 25. Supplementary functions for Gaussian basis sets *J. Chem. Phys.* **80** 3265

[49] Neese F 2003 An improvement of the resolution of the identity approximation for the formation of the Coulomb matrix *J. Comput. Chem.* **24** 1740
[50] Neese F, Wennmohs F, Hansen A and Becker U 2009 Efficient, approximate and parallel Hartree-Fock and hybrid DFT calculations. A 'chain-of-spheres' algorithm for the Hartree-Fock exchange *Chem. Phys.* **356** 98
[51] Stoychev G L, Auer A A and Neese F 2017 Automatic generation of auxiliary basis sets *J. Chem. Theory Comput.* **13** 554
[52] Koseki S, Schmidt M W and Gordon M S 1992 MCSCF/6-31G(d,p) calculations of one-electron spin-orbit coupling constants in diatomic molecules *J. Phys. Chem.* **96** 10768
[53] Koseki S, Gordon M S, Schmidt M W and Matsunaga N 1995 Main group effective nuclear charges for spin-orbit calculations *J. Phys. Chem.* **99** 12764
[54] Koseki S, Schmidt M W and Gordon M S 1998 Effective nuclear charges for the first- through third-row transition metal elements in spin-orbit calculations *J. Phys. Chem.* A **102** 10430
[55] Rudowicz C and Misra S K 2001 Spin-Hamiltonian formalisms in electron magnetic resonance (EMR) and related spectroscopies *Appl. Spectrosc. Rev.* **36** 11
[56] Neese F 2017 Quantum chemistry and EPR parameters *eMagRes* **6** 1
[57] Sayfutyarova E R and Chan G K-L 2018 Electron paramagnetic resonance g-tensors from state interaction spin-orbit coupling density matrix renormalization group *J. Chem. Phys.* **148** 184103
[58] Malkina O L, Vaara J, Schimmelpfennig B, Munzarová M, Malkin V G and Kaupp M 2000 Density functional calculations of electronic g-tensors using spin-orbit pseudopotentials and mean-field all-electron spin-orbit operators *J. Am. Chem. Soc.* **122** 9206
[59] Neese F 2001 Prediction of electron paramagnetic resonance g values using coupled perturbed Hartree-Fock and Kohn-Sham theory *J. Chem. Phys.* **115** 11080
[60] Rinkevicius Z, Telyatnyk L, Sałek P, Vahtras O and Ågren H 2003 Restricted density-functional linear response theory calculations of electronic g-tensors *J. Chem. Phys.* **119** 10489
[61] Gauss J, Kállay M and Neese F 2009 Calculation of electronic g-tensors using coupled cluster theory *J. Phys. Chem.* A **113** 11541
[62] Franzke Y J and Yu J M 2022 Quasi-relativistic calculation of EPR g tensors with derivatives of the decoupling transformation, gauge-including atomic orbitals, and magnetic balance *J. Chem. Theory Comput.* **18** 2246
[63] Shames A I and Panich A M 2017 Paramagnetic defects in nanodiamonds *Nanodiamonds: Advanced Material Analysis, Properties and Applications* (Elsevier) ch. 6 pp 131–54
[64] Eldemrdash S *et al* 2023 Fluorescent HPHT nanodiamonds have disk- and rod-like shapes *Carbon* **206** 268
[65] Fehr M *et al* 2011 Combined multifrequency EPR and DFT study of dangling bonds in *a*-Si:H *Phys. Rev.* B **84** 245203
[66] Paleari S, Baldovino S, Molle A and Fanciulli M 2013 Evidence of trigonal dangling bonds at the Ge(111)/oxide interface by electrically detected magnetic resonance *Phys. Rev. Lett.* **110** 206101